CHAPTER 5
TRANSITION METAL-DECORATED C_{18} AS A CO, NO, AND NH_3 SCAVENGER

5.1. INTRODUCTION

Carbon, with its diverse properties, has become a crucial material for various applications, including conducting polymers, thin solid diamond sheets, nanotubes, fullerenes, and various carbon clusters. The 2019 synthesis of the C_{18} nanocluster, an 18-carbon sp-hybridized ring [1-2], has garnered significant interest due to its remarkable reactivity. The presence of toxic gases, such as carbon monoxide (CO) and nitric oxide (NO), poses a significant threat to indoor spaces. As a result, there is a growing demand for gas sensors that are cost-effective and highly sensitive, capable of swiftly detecting these hazardous gases. Various carbon nanostructures, such as C_{60}, graphene, carbon dots, nanotubes, and nano-rings, have been explored [3-6] for their potential in detecting CO, NO, and ammonia (NH_3).

Transition metals, known for their partially filled d-orbitals, provide a unique opportunity for impurity decoration, enhancing adsorption through orbital interactions and enabling charge transfer [7]. Present chapter investigates transition metal decoration using Ni, Pd, and Pt on the edge of C_{18} nanoclusters, focusing on structural properties like bond lengths and angles. It also investigates electronic properties using density of states analysis, Mulliken charge analysis, and spectroscopic qualities such as infrared (IR) and Raman spectra. The exploration extends to the realm of quantum theory of atoms in molecules (QTAIM) with non-covalent interaction (NCI) analysis, providing deeper insights into atomic interactions.

5.2. METHODOLOGY

First principles-based density functional theory (DFT) calculations were conducted using the Gaussian 09 package [8]. The range-separated hybrid ωB97XD was chosen for optimizing the C_{18}TM (TM = Ni, Pd, Pt) nanoclusters due to its accurate reproduction of the experimentally observed structural geometry of polyynic C_{18} [9]. All geometry optimizations were carried out using the LanL2DZ Gaussian basis set, given the transition metal impurities [10]. The same level of theory was applied to compute total energies, electronic parameters, molecular orbitals (MO), recovery time, Raman spectra, and adsorption energies. The visualization of structural geometry was performed using GaussView (version 6), based on the results of DFT calculations. MO plots were generated using the GaussSum tool. For the visualization of non-covalent interactions, the visual molecular dynamics (VMD) software [11] has been employed; for the plotting of reduced density gradient, *Multiwfn* package [12] has been employed. Throughout the calculations, convergence criteria were maintained at 12×10^{-4} radians, 18×10^{-4} Bohr, 3×10^{-4} Hartree/radian, and 45×10^{-5} Hartree/Bohr for gradients of root-

mean-square (rms) displacement, maximum displacement, rms force, and maximum force, respectively.

The HOMO-LUMO gap (E_G), representing the difference between the highest occupied molecular orbital (HOMO) and the lowest unoccupied molecular orbital (LUMO), was determined as follows [13]:

$$E_G = E_{LUMO} - E_{HOMO} \text{ ----- (1)}$$

Where E_{LUMO} and E_{HOMO} denote the LUMO energy and HOMO energy, respectively. The Fermi level energy (E_F) was calculated using the following relation [14]:

$$E_F = (E_{LUMO} + E_{HOMO})/2 \text{ ----- (2)}$$

5.3. RESULTS AND DICUSSION

5.3.1. Structural and Electronic Properties of TM-decorated C_{18} Nanocluster

To enhance the adsorption performance of the pristine C_{18} nanocluster, we have introduced three transition metal (TM) atoms: Nickel (Ni), Palladium (Pd), and Platinum (Pt), as impurity decorations. These TM atoms exhibit a strong interaction with the C_{18} nanocluster. To corroborate this strong interaction, we calculated the binding energy (E_b) of the resulting nanoclusters, namely $C_{18}Ni$, $C_{18}Pd$, and $C_{18}Pt$, formed after decorating C_{18} with these TM atoms (see *Figure 5.1*). The binding energy (E_b) is determined using the formula [15]:

$$E_b = E(C_{18}TM) - E(C_{18}) - E(TM) \text{ ---- (3)}$$

Where, TM represents the transition metals Ni, Pd, and Pt. The computed E_b values are: -4.19 eV for $C_{18}Ni$, -1.83 eV for $C_{18}Pd$, and -3.19 eV for $C_{18}Pt$ nanoclusters. Negative E_b values indicate a strong and favourable interaction between the C_{18} nanocluster and the transition metal atoms. The average lengths of C-C single bonds are 1.37 Å and 1.24 Å for the triple bond in the case of $C_{18}Ni$ nanocluster. In the $C_{18}Pd$ and $C_{18}Pt$ nanoclusters, the average carbon-carbon single bond lengths are 1.36 Å, and the carbon-carbon triple bond lengths are 1.24 Å. In all three cases, the impurity TM atoms form chemical bonds with the C_{18} nanocluster, resulting in binding lengths of 1.85 Å for $C_{18}Ni$, 2.06 Å for $C_{18}Pd$, and 2 Å for $C_{18}Pt$ nanoclusters. *Table 5.1* provides a summary of bond lengths, binding distances, and binding energies for the $C_{18}TM$ nanoclusters.

To gain insight into how the decoration affects changes in bond lengths and angles, we have plotted graphs illustrating the alterations in bond length (BLA) and angle (AA) (refer to the *Figure 2*). We observed the most significant BLA in the $C_{18}Ni$ nanocluster, followed by $C_{18}Pt$ and then $C_{18}Pd$. Similarly, the highest degree of AA was observed in the $C_{18}Ni$ nanocluster, followed by $C_{18}Pt$ and $C_{18}Pd$ nanoclusters. In order to assess the structural stability of $C_{18}TM$ nanoclusters, we computed their formation energies (E_{Form}) using the following equation [16]:

$$E_{Form} = \frac{E(C_{18}TM) - N*E(C) - E(TM)}{N+1} \text{ ---- (4)}$$

Here, N equals 18. The calculated formation energies are as follows: -7.42 eV/atom for $C_{18}Ni$, -7.29 eV/atom for $C_{18}Pd$, and -7.36 eV/atom for $C_{18}Pt$ nanoclusters. The negative values of formation energy indicate the stability of $C_{18}Ni$, $C_{18}Pd$, and $C_{18}Pt$ nanoclusters.

Additionally, we conducted simulations of the infrared (IR) spectra for the TM-decorated nanoclusters. In the obtained IR spectra, all frequencies are positive. This positive frequency distribution suggests the potential for the natural existence of $C_{18}Ni$, $C_{18}Pd$, and $C_{18}Pt$ nanoclusters. *Figure 5.3* shows the IR spectra for $C_{18}Ni$, $C_{18}Pd$, and $C_{18}Pt$ nanoclusters.

We calculated molecular orbital (MO) spectra, also known as density of states plots, to get a better understanding of the electronic properties. Analysis of these MO spectra reveals that for the $C_{18}Ni$ nanocluster, the HOMO and LUMO energies are recorded as -7.80 eV and -1.35 eV, respectively. This information implies that the energy gap (E_G) and the Fermi energy (E_F) for this nanocluster stand at 6.45 eV and -4.57 eV, respectively. As for the $C_{18}Pd$ nanocluster, the values for E_{HOMO}, E_{LUMO}, E_G, and E_F are found to be -7.92 eV, -1.50 eV, 6.42 eV, and -4.71 eV, respectively. Likewise, for the $C_{18}Pt$ nanocluster, the corresponding values are -7.86 eV, -1.75 eV, 6.11 eV, and -4.80 eV, respectively.

Table 5.1: bond lengths, binding distances, binding energies for $C_{18}TM$ nanoclusters.

System	Bond Length (Å)		Binding Length (Å)	Binding Energy (eV)
	$C-C$	$C \equiv C$		
$C_{18}Ni$	1.37	1.24	1.85	-4.19
$C_{18}Pd$	1.36	1.24	2.06	-1.83
$C_{18}Pt$	1.36	1.24	2.00	-3.19

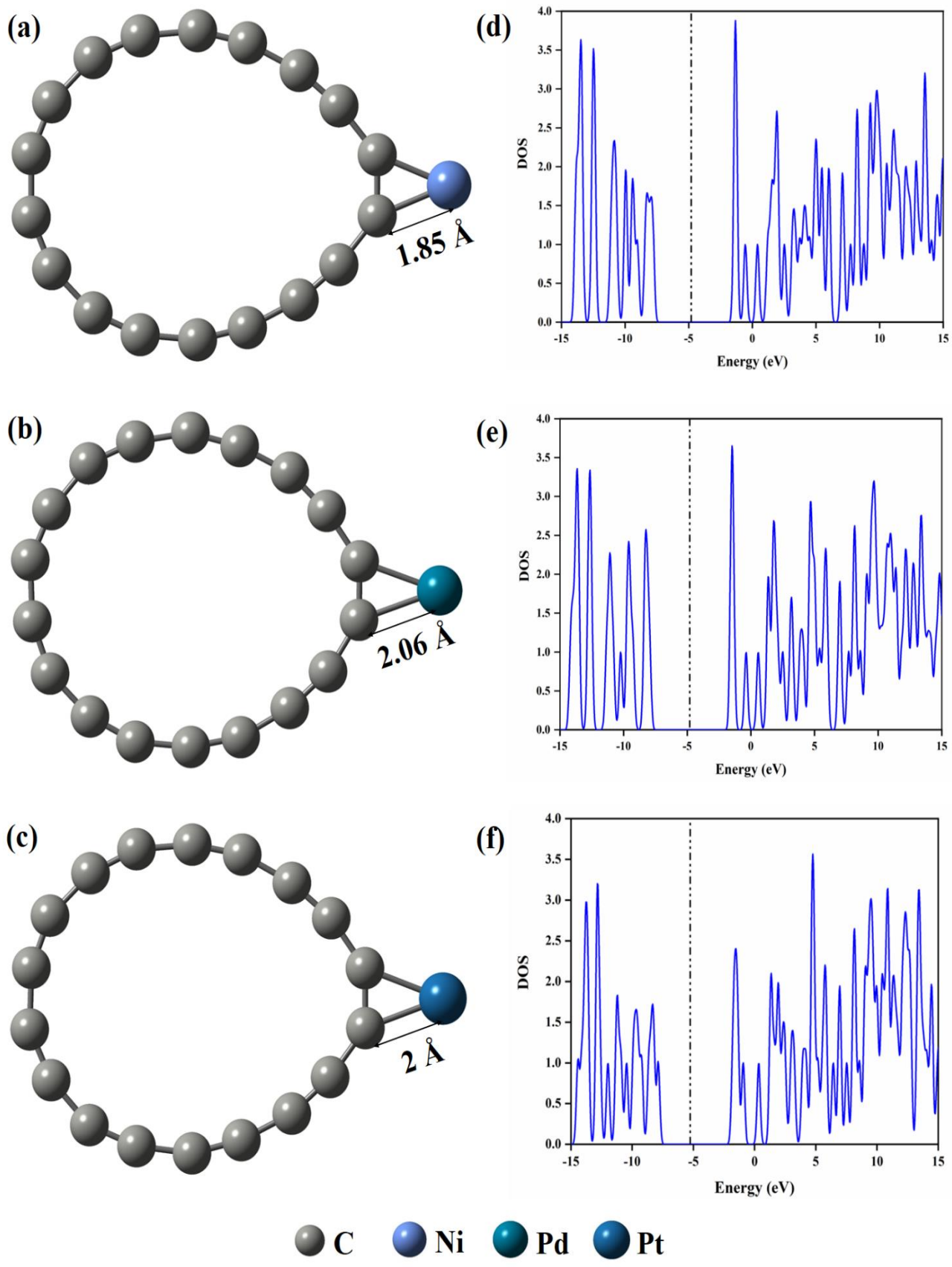

Figure 5.1: (a, b, c): optimized geometries (d, e, f) molecular orbital spectra for $C_{18}TM$ nanoclusters

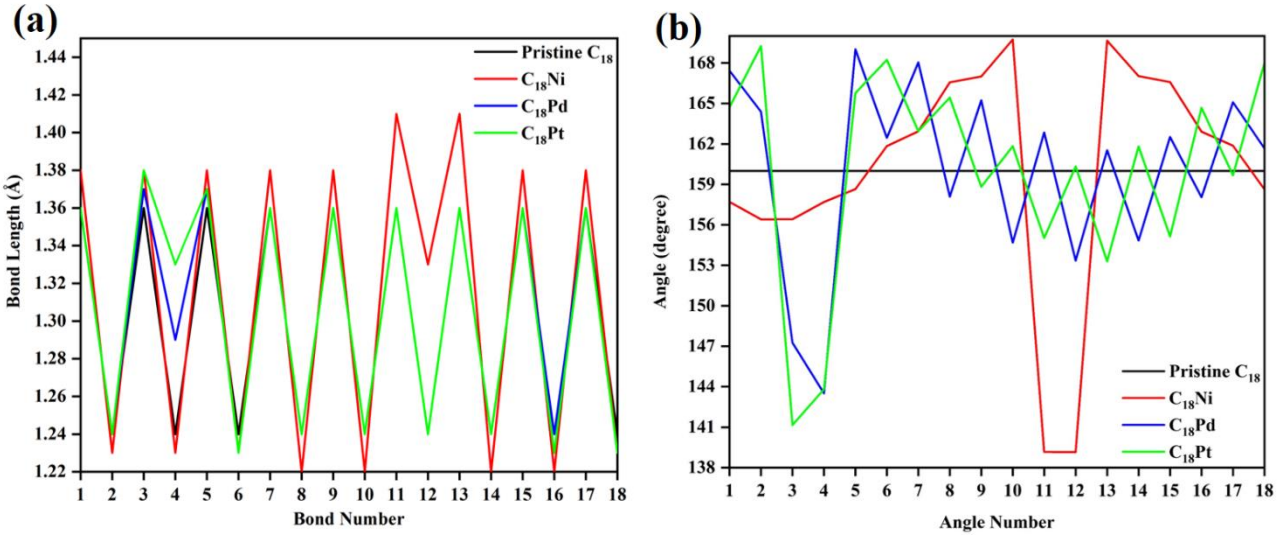

Figure 5.2: (a) Bond length alteration (BLA) (b) angle alteration (AA) plots for C_{18}TM nanoclusters

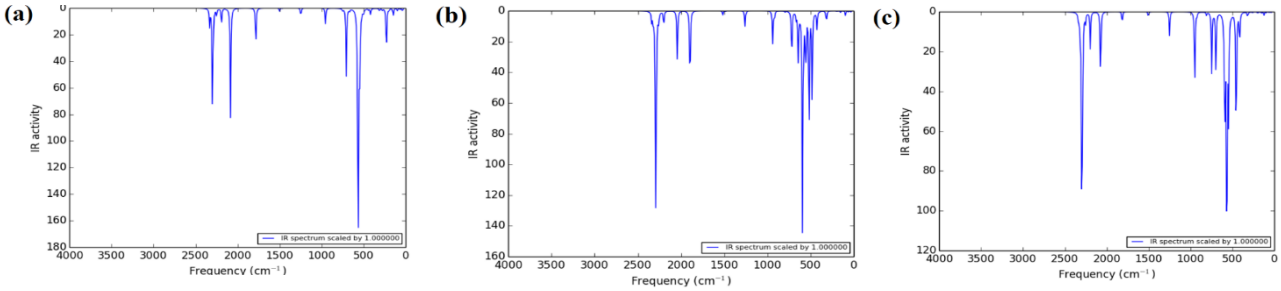

Figure 5.3: IR spectra for (a) C_{18}Ni (b) C_{18}Pd (c) C_{18}Pt nanoclusters

5.3.2. Adsorption Properties of TM-decorated C_{18} Nanocluster

According to the molecular electrostatic potential (MESP) maps, we have identified that the most reactive site on a C_{18}TM nanocluster is in close proximity to the impurity atom. We experimented with three different orientations of CO, NO, and NH_3 molecules and selected the one with the lowest energy, signifying its stability, for further calculations. The adsorption energy is given by:

$$E_{ad} = E(C_{18}TM + gas) - E(C_{18}TM) - E(gas) \text{ ---- (3)}$$

The computed values of adsorption energies are -1.98 eV, -1.96 eV, and -1.89 eV for the CO, NO, and NH_3 adsorption over the C_{18}Ni nanocluster. Whereas the final separation after the CO, NO, and NH_3 adsorption (a.k.a the adsorption distances) are 1.78 Å, 1.72 Å, and 1.98 Å (see Figure 4). To get a better understanding of electronic properties we have calculated HOMO and LUMO energies, energy gap (E_G), and Fermi level (E_F), along with the molecular orbital (MO) spectra. The HOMO energies for CO and NH_3 adsorption are -8.32 eV and -7.36

eV respectively. And the LUMO energies are -1.77 eV and -0.99 eV. Which makes the E_G to be 6.55 eV for CO adsorption and 6.37 eV for the NO adsorption. And the E_F is -3.27 eV and -4.17 eV for CO and NH_3, respectively. However, in case of NO adsorption the molecular orbitals split into alpha (α) and beta (β) MOs. The HOMO energy is -8.11 eV for α and -8.47 eV for β-MO. The E_{LUMO} is -1.93 eV for α and -2.29 eV for β-MO. Implies that the E_G is 6.18 eV for both alpha and beta. While the E_F is -5.02 eV for α and -5.38 eV for β-MO.

Regarding the adsorption performance of the $C_{18}Pd$ nanocluster, we have employed a similar approach as with the $C_{18}Ni$ nanocluster. The active site selection was based on the MESP maps, followed by the selection of three orientations for each gas molecule. From these orientations, we have chosen the configurations with the lowest energy for subsequent calculations. The adsorption energy values calculated from the equation (3) are -1.55 eV, -1.09 eV, and -1.41 eV, for CO, NO, and NH_3 adsorptions, respectively. The separation following the adsorption of CO, NO, and NH_3 molecules, also referred to as adsorption distance, measures 1.72 Å, 1.95 Å, and 2.20 Å (as depicted in *Figure 5.5*).

In order to gain a deeper insight into the electronic properties, we conducted calculations for HOMO and LUMO energies, energy gap (E_G), and Fermi level (E_F), and the MO spectra. For CO and NH_3 adsorption, the HOMO energies were determined to be -8.24 eV and -7.51 eV, respectively, while the LUMO energies were -1.80 eV and -0.1.16 eV, respectively. Consequently, this results in an energy gap (E_G) of 6.44 eV for CO adsorption and 6.35 eV for NO adsorption. The Fermi level (E_F) was found to be -5.07 eV for CO and -4.33 eV for NH3. Whereas, in the case of NO adsorption, the molecular orbitals split into alpha (α) and beta (β) MOs. The HOMO energy was measured at -8.26 eV for α and -8.36 eV for β-MO, while the E_{LUMO} was -2.12 eV for α and -2.05 eV for β-MO. Consequently, this leads to an energy gap (E_G) of 6.14 eV for alpha and 6.31 eV for beta. The E_F was determined to be -5.19 eV for α and -5.20 eV for β-MO in the case of NO adsorption.

Subsequent to the investigation of $C_{18}Ni$ and $C_{18}Pd$, a parallel approach was employed to assess the adsorption performance of $C_{18}Pt$. This approach involved the initial selection of active sites using the MESP maps, followed by the consideration of three distinct orientations for each gas molecule. From these orientations, we identified and retained the configurations with the lowest energy levels for subsequent calculations. Consequently, the computed adsorption energy values, as determined by Equation (3), amounted to -2.31 eV, -1.87 eV, and -1.99 eV for the adsorption of CO, NO, and NH_3, respectively. Following the adsorption of

CO, NO, and NH_3 molecules, the consequent separation, termed the adsorption distance, measures 1.89 Å, 1.87 Å, and 2.14 Å (as seen in *Figure 5.6*).

In our pursuit of the electronic parameters, we once again undertook computations encompassing HOMO and LUMO energies, energy gap (E_G), Fermi level (E_F), and molecular orbital (MO) spectra analysis. For CO and NH_3 adsorption scenarios, the HOMO energies were ascertained to be -8.30 eV and -7.38 eV, respectively, while the LUMO energies registered at -2.03 eV and -1.18 eV, respectively. As a result, these findings give rise to energy gap (E_G) values of 6.27 eV for CO adsorption and 6.21 eV for NO adsorption. Furthermore, the Fermi level (E_F) exhibited measurements of -5.16 eV for CO and -4.28 eV for NH_3. Intriguingly, within the context of NO adsorption, the molecular orbitals exhibit a splitting into alpha (α) and beta (β) MOs. The HOMO energy levels were recorded as -8.30 eV for α and -8.43 eV for β-MO, while the E_{LUMO} values stood at -2.21 eV for α and -2.24 eV for β-MO. Consequently, these results translate into energy gap (E_G) values of 6.09 eV for alpha and 5.98 eV for beta. Moreover, the E_F was calculated as -5.25 eV for α and -5.44 eV for β-MO in the context of NO adsorption. Table 5.2 presents data regarding adsorption energies, HOMO-LUMO energy levels, energy gaps, and Fermi levels following the adsorption of CO, NO, and NH_3 onto C_{18}TM nanoclusters.

Table 5.2: adsorption energies, HOMO-LUMO energy levels, energy gaps, and Fermi levels following the adsorption of CO, NO, and NH_3 onto C_{18}TM nanoclusters.

System	E_{ad} (eV)	E_{HOMO} (eV)	E_{LUMO} (eV)	E_G (eV)	E_F (eV)
CO/C_{18}Ni	-1.98	-8.32	-1.77	6.55	-3.27
NO/C_{18}Ni	-1.96	-8.11(α) -8.47(β)	-1.93(α) -2.29(β)	6.18(α) 6.18(β)	-5.02(α) -5.38(β)
NH_3/C_{18}Ni	1.89	-7.36	-0.99	6.37	-4.17
CO/C_{18}Ni	-1.55	-8.24	-1.80	6.44	-5.02
NO/C_{18}Pd	-1.09	-8.26(α) -8.36(β)	-2.12(α) -2.05(β)	6.14(α) 6.31(β)	-5.19(α) -5.20(β)
NH_3/C_{18}Pd	-1.41	-7.51	-1.16	6.35	-4.33
CO/C_{18}Pt	-2.31	-8.30	-2.03	6.27	-5.16
NO/C_{18}Pt	-1.87	-8.30(α) -8.43(β)	-2.21(α) -2.24(β)	6.09(α) 5.98(β)	-5.25(α) -5.44(β)
NH_3/C_{18}Pt	-1.99	-7.38	-1.18	6.21	-4.28

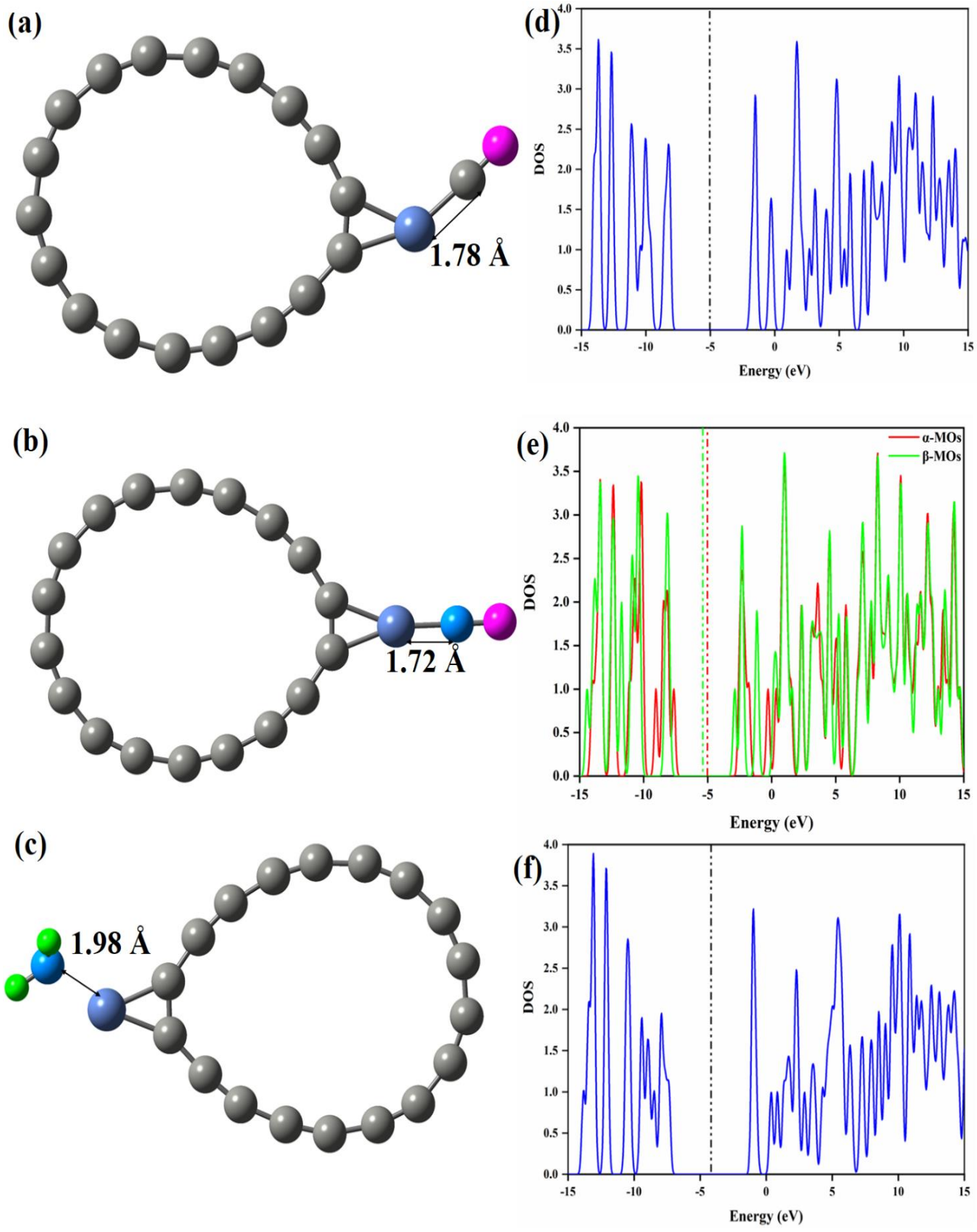

Figure 5.4: (a, b, c) minimum energetic configurations (d, e, f) molecular orbital spectra of $C_{18}Ni$ nanocluster after CO, NO, NH_3 adsorption

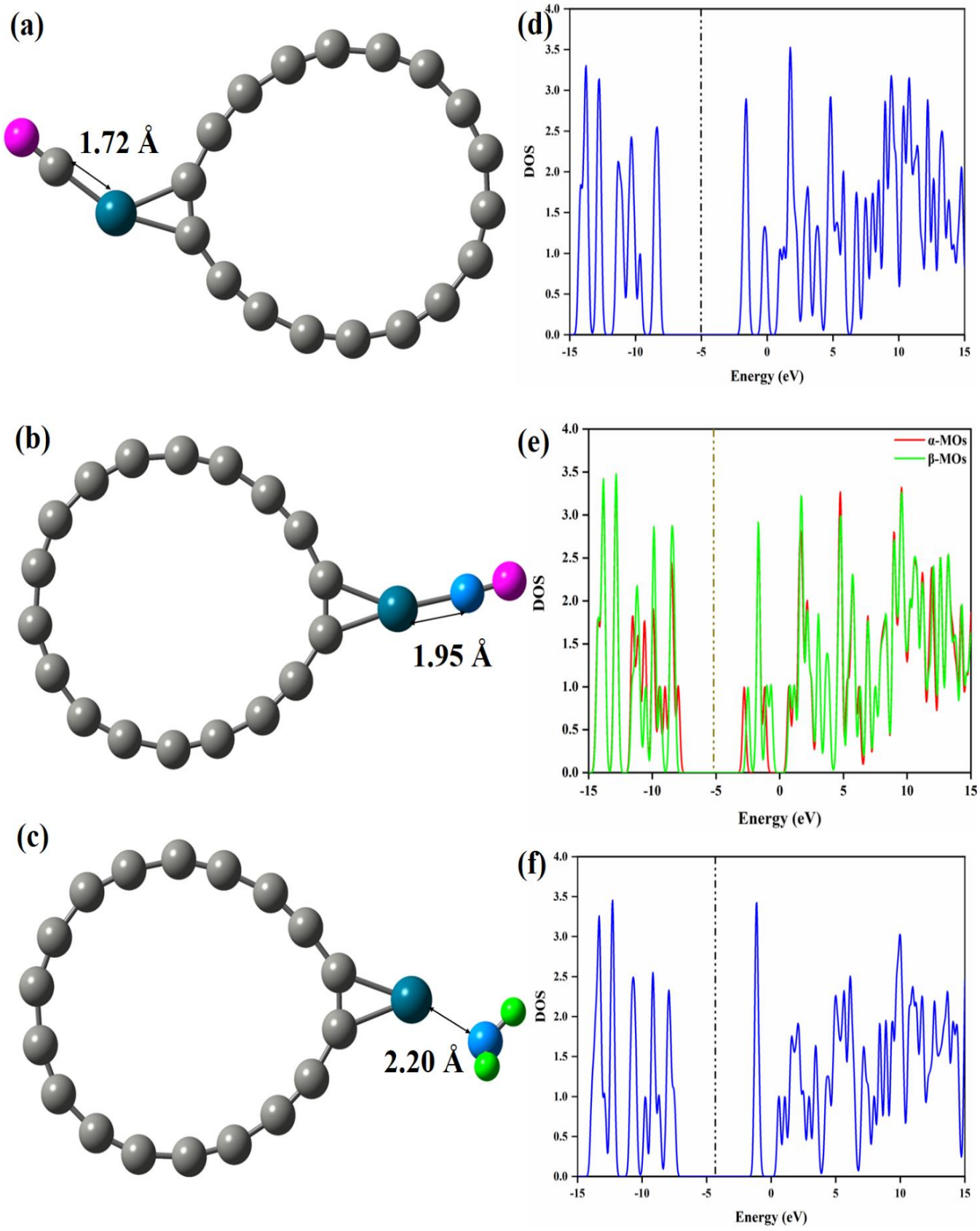

Figure 5.5: (a, b, c) minimum energetic configurations (d, e, f) molecular orbital spectra of $C_{18}Pd$ nanocluster after CO, NO, NH_3 adsorption

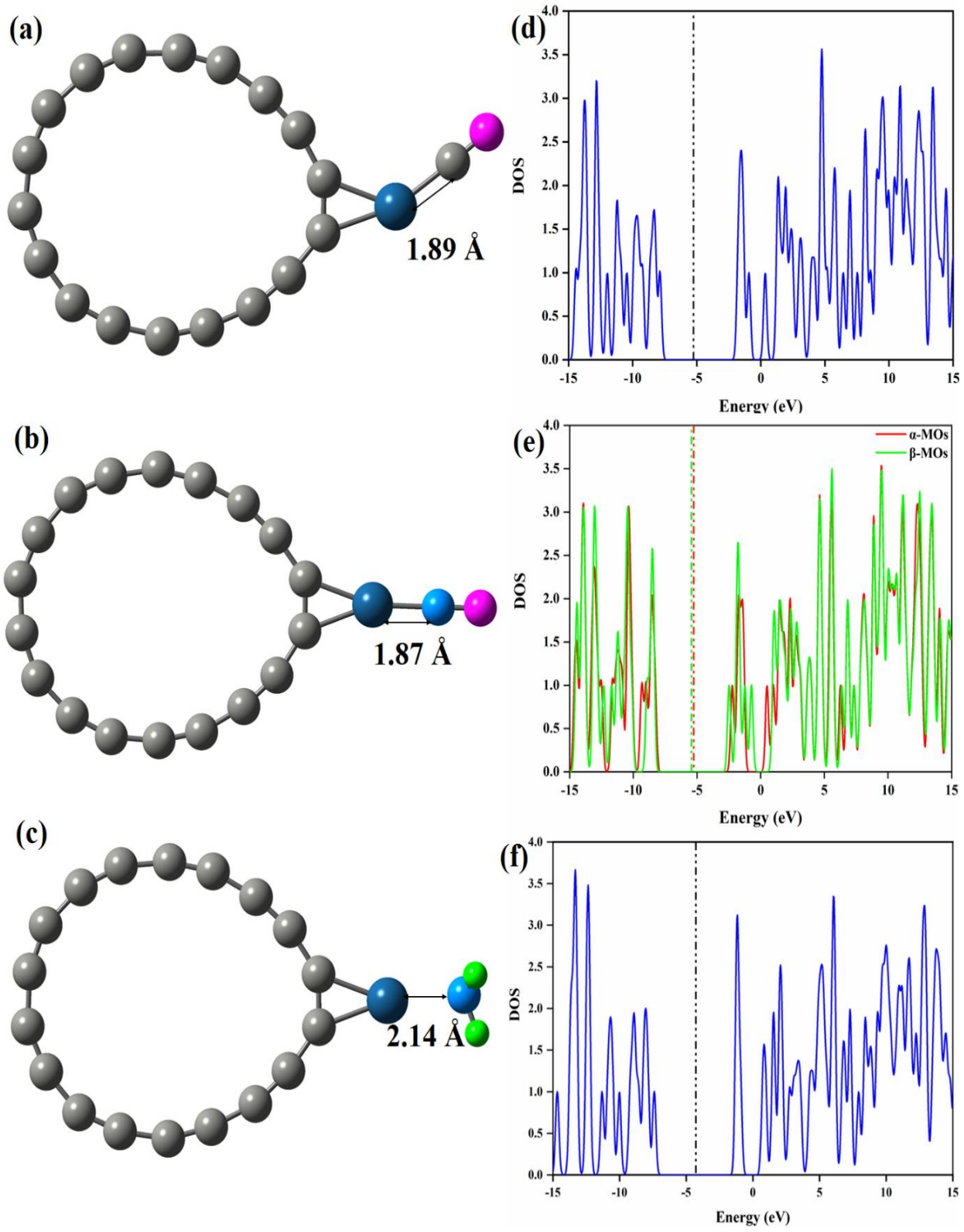

Figure 5.6: (a, b, c) minimum energetic configurations (d, e, f) molecular orbital spectra of $C_{18}Pt$ nanocluster after CO, NO, NH_3 adsorption

5.3.3. Mulliken Charge Population Analysis

Mulliken analysis was employed to assess the charge distribution before and after adsorption, enabling the determination of the direction of charge transfer. In the case of C18Ni nanocluster, the charges evolved to -0.056e, -0.288e, and +0.167e for CO, NO, and NH3 adsorptions, respectively. Similarly, for $C_{18}Pd$ nanocluster, the charges changed to -0.036e, -0.070e, and +0.146e for CO, NO, and NH_3 adsorptions, respectively. Likewise, for $C_{18}Pt$, the charge transformations yielded -0.234e, -0.246e, and +0.162e for CO, NO, and NH_3 adsorptions, respectively. It's noteworthy that the final charges on the CO and NO molecules were consistently negative in all three cases, while the final charge on the NH_3 molecule consistently remained positive. This positive final charge indicates a transfer of charge from the NH_3 molecule to the nanoclusters, while negative sign suggests the charge transfer being the other way around [13]. *Figure 5.7* provides the Mulliken atomic charge distributions (MACD) following the adsorption of CO, NO, and NH_3 for $C_{18}TM$ nanoclusters.

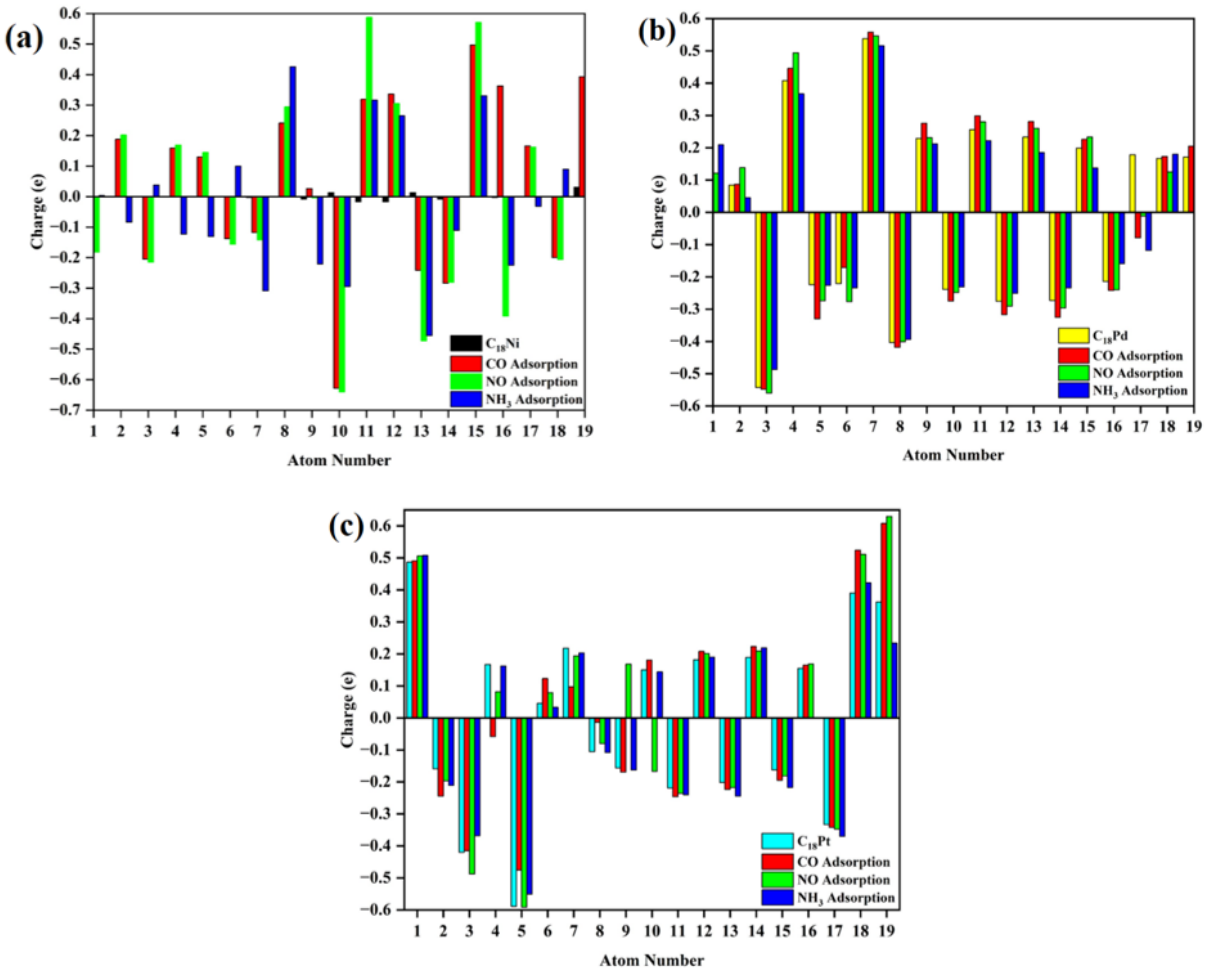

Figure 5.7: Mulliken atomic charge distributions of $C_{18}TM$ nanoclusters after CO, NO, NH_3 adsorption

5.3.4. Quantum Theory of Atoms in Molecules (QTAIM) Study

To get deep interaction insights between gas molecules and TM-decorated C_{18}, we conducted a topological analysis utilizing Bader's quantum theory of atoms in molecules (QTAIM) method with the Multiwfn package [17]. This analysis encompasses crucial parameters: electron density ρ(r), Laplacian $\nabla^2\rho(r)$, total energy density H(r), and the ratio |V(r)| / (G(r)), which serve to characterize a spectrum of interactions. The QTAIM analysis [18] unveils distinctive attributes associated with these interactions. When $\nabla^2\rho(r) > 0$, H(r) > 0, and |V(r)| / (G(r)) < 1, it indicates the presence of weak to medium-strength hydrogen bonds and Van der Waals interactions. In the case of strong hydrogen bonds, a middle ground interaction type emerges, characterized by $\nabla^2\rho(r) > 0$, H(r) < 0, and 1 < |V(r)| / (G(r)) < 2. Conversely, covalent bonds exhibit features where $\nabla^2\rho(r) < 0$, H(r) < 0, and |V(r)| / (G(r)) >2 [19].

Table 5.3: electron density, Laplacian, total energy density, and the ratio |V(r)| / (G(r)),

System	CP No.	ρ_{BCP}	G_{BCP}	H_{BCP}	V_{BCP}	$\nabla^2\rho_{BCP}$	$\frac{\lvert V_{BCP}\rvert}{G_{BCP}}$
$CO/C_{18}Ni$	31	0.1361	0.2238	0.0588	-0.2827	0.6602	1.2632
$NO/C_{18}Ni$	31	0.1506	0.2858	0.0630	-0.3488	0.8909	1.2204
$NH_3/C_{18}Ni$	37	0.0858	0.1268	0.0179	-0.1446	0.4357	1.1404
$CO/C_{18}Pd$	31	0.1065	0.1137	0.0203	-0.1340	0.3736	1.1785
$NO/C_{18}Pd$	36	0.3822	0.2341	0.5017	-0.7359	-0.107	3.1328
$NH_3/C_{18}Pd$	38	0.0569	0.0598	0.002648	-0.0625	0.2288	1.0451
$CO/C_{18}Pt$	35	0.1409	0.1744	0.04809	-0.2225	0.5288	1.2758
$NO/C_{18}Pt$	34	0.1268	0.1995	0.02305	-0.2225	0.7417	1.1153
$NH_3/C_{18}Pt$	33	0.0859	0.0846	0.0167	-0.1014	0.2790	1.1986

Table 5.3 offers an insight into the computed QTAIM parameters for TM-decorated C_{18}, while *Figure 5.8* provides a visual representation of molecular topographical maps featuring critical interaction points for gas molecules. These analyses unveil four distinct interaction types between the gas molecule and the system. Notably, the interaction of NH_3 with $C_{18}Ni$, $C_{18}Pd$, and $C_{18}Pt$ nanoclusters demonstrates lower ρ values, indicative of weaker interactions compared to other interactions. The V(r)/G(r) ratio falls between 1 and 2 for all interactions

except NO/C_{18}Pd, suggesting a covalent interaction, while the rest are categorized as intermediate interactions.

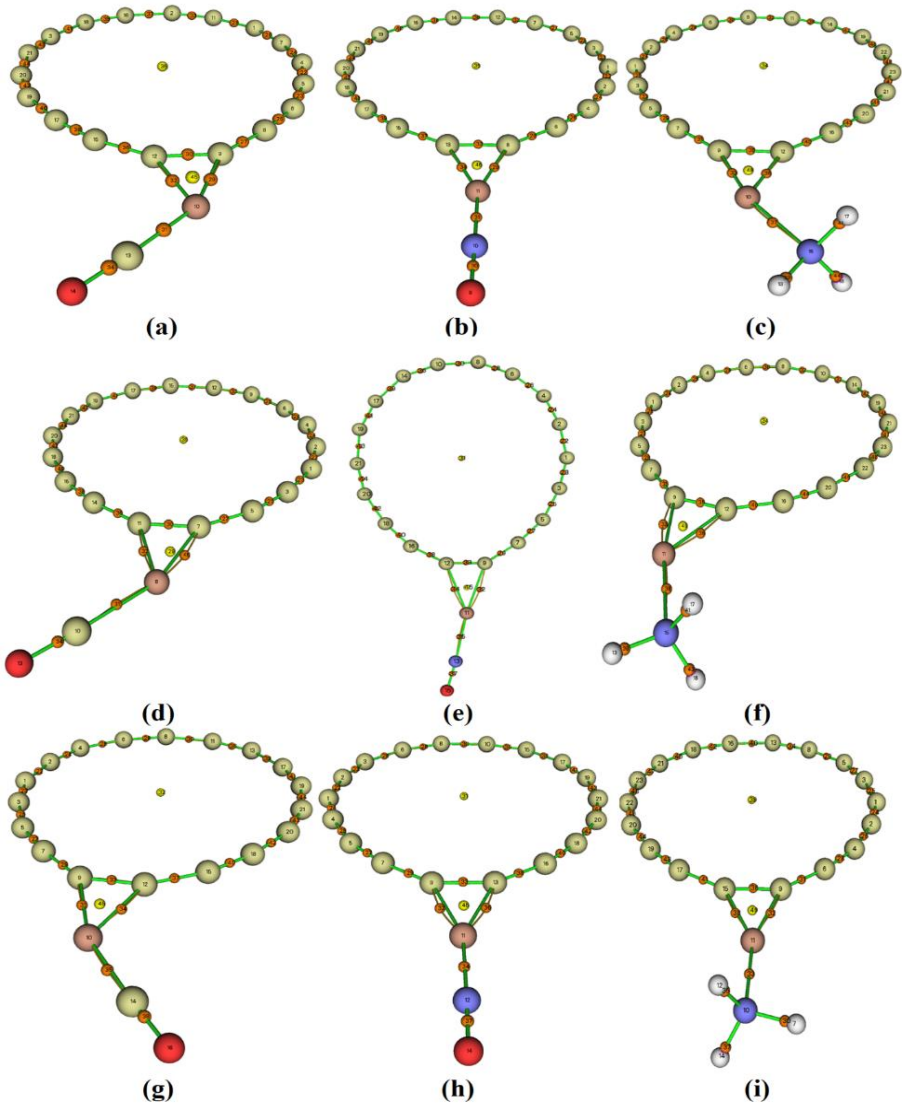

Figure 5.8: Molecular topographical maps for C_{18}TM nanoclusters after CO, NO, and NH_3 adsorption

5.3.5. Reduced Density Gradient and Non Covalent Interactions

Reduced Density Gradient (RDG) plots serve as a valuable analytical tool for comprehending the attractive and repulsive aspects of molecular interactions and evaluating their strength [20-21]. The sign (λ_2) values within these plots carry significant information; positive values indicate robust attractive forces within the charge density, while negative values signify repulsive forces. When ρ equals 0, it corresponds to van der Waals forces. In the context of Non-Covalent Interaction (NCI) diagrams, distinctive regions color-coded as blue, green,

and red represent strong interactions, van der Waals interactions, and intense steric interactions, respectively, as illustrated in *Figures 5.9, 5.10, and 5.11*. The interactions between gas molecules and C_{18}TM nanoclusters are notably associated with van der Waals interactions [22].

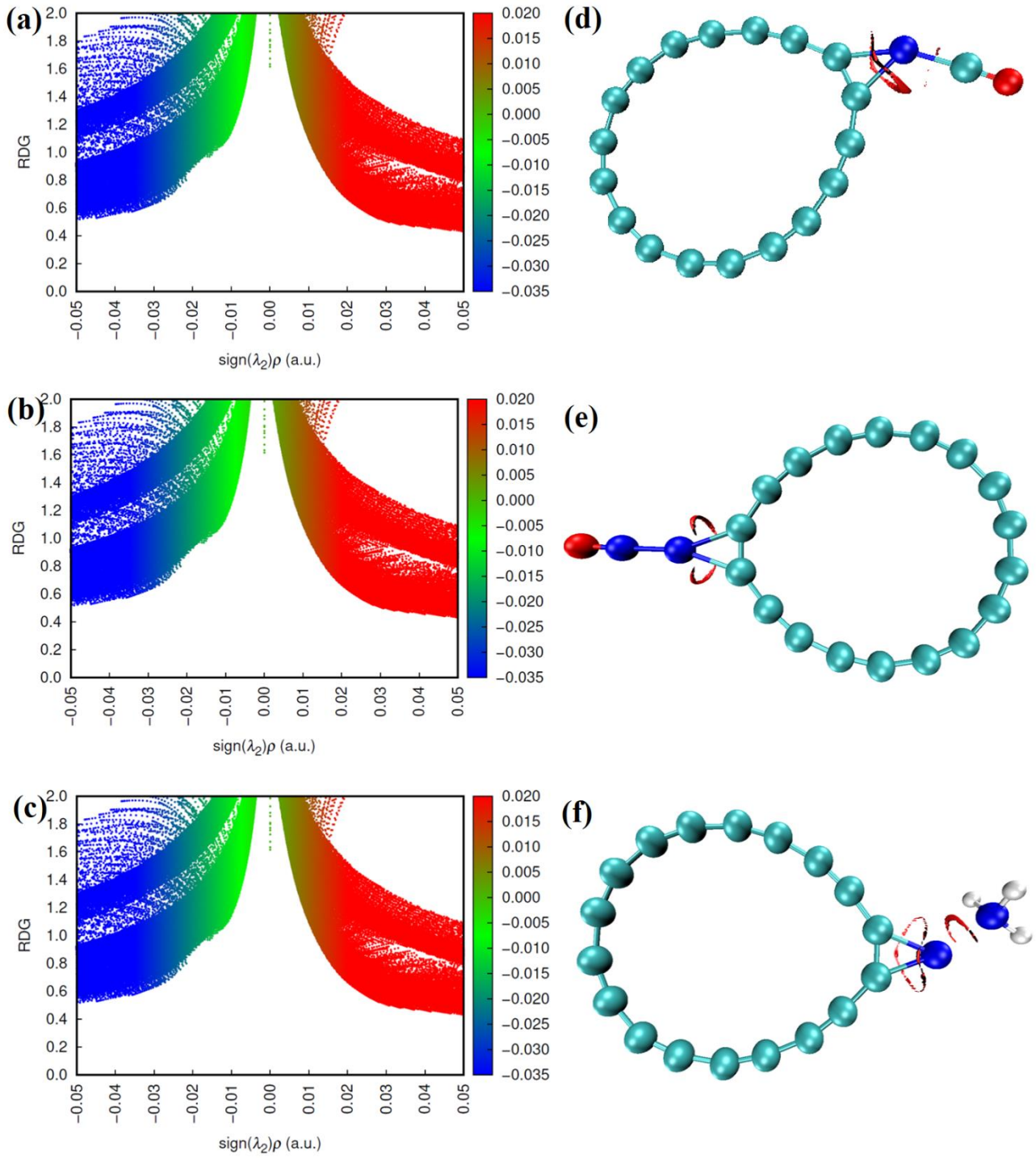

Figure 5.9: (a, b, c) reduced density gradient (RDG) plots and (d, e, f) non-covalent interaction (NCI) diagrams for C_{18}Ni nanocluster after CO, NO, and NH_3 adsorption

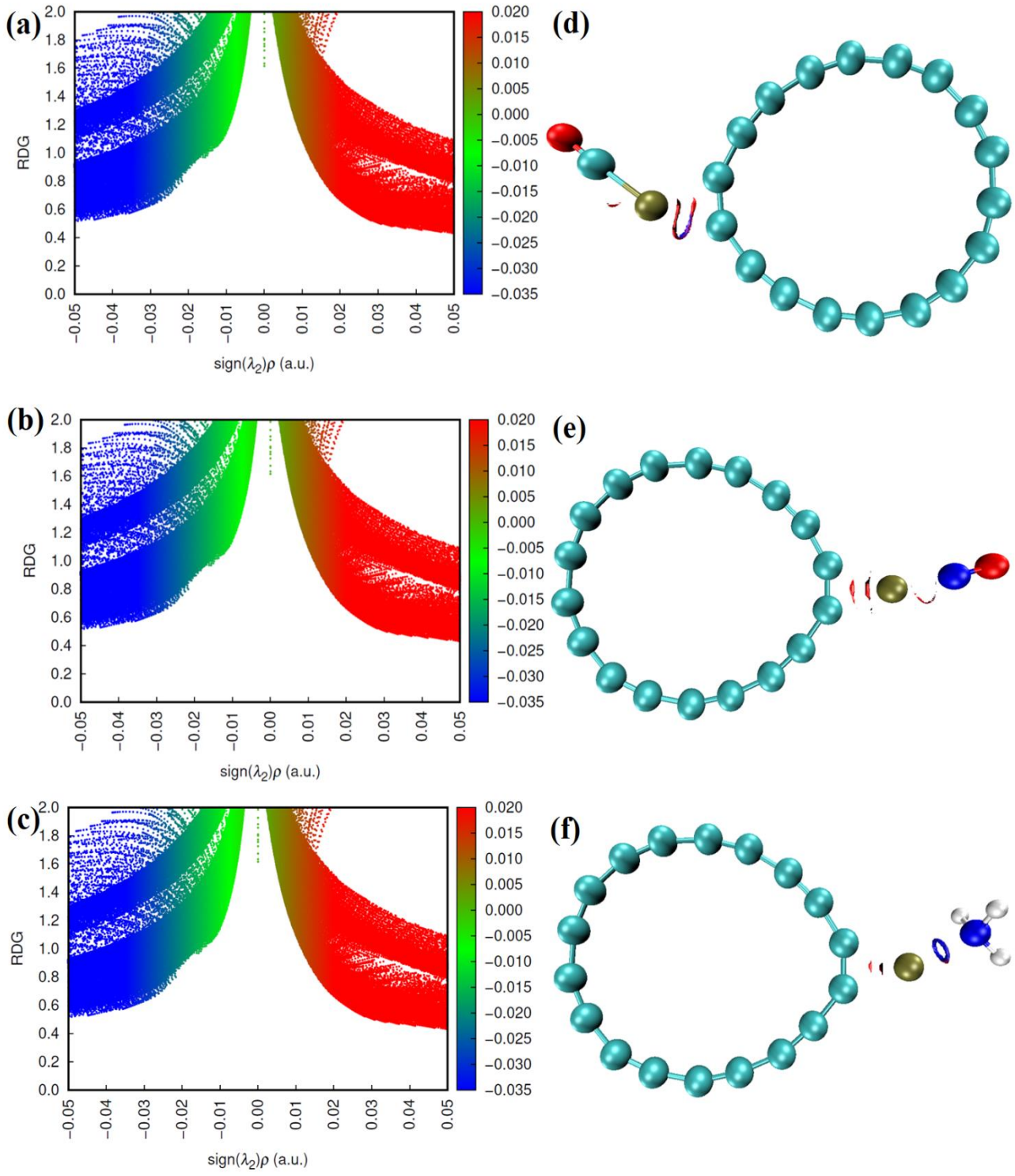

Figure 5.10: (a, b, c) reduced density gradient (RDG) plots and (d, e, f) non-covalent interaction (NCI) diagrams for $C_{18}Pd$ nanocluster after CO, NO, and NH_3 adsorption

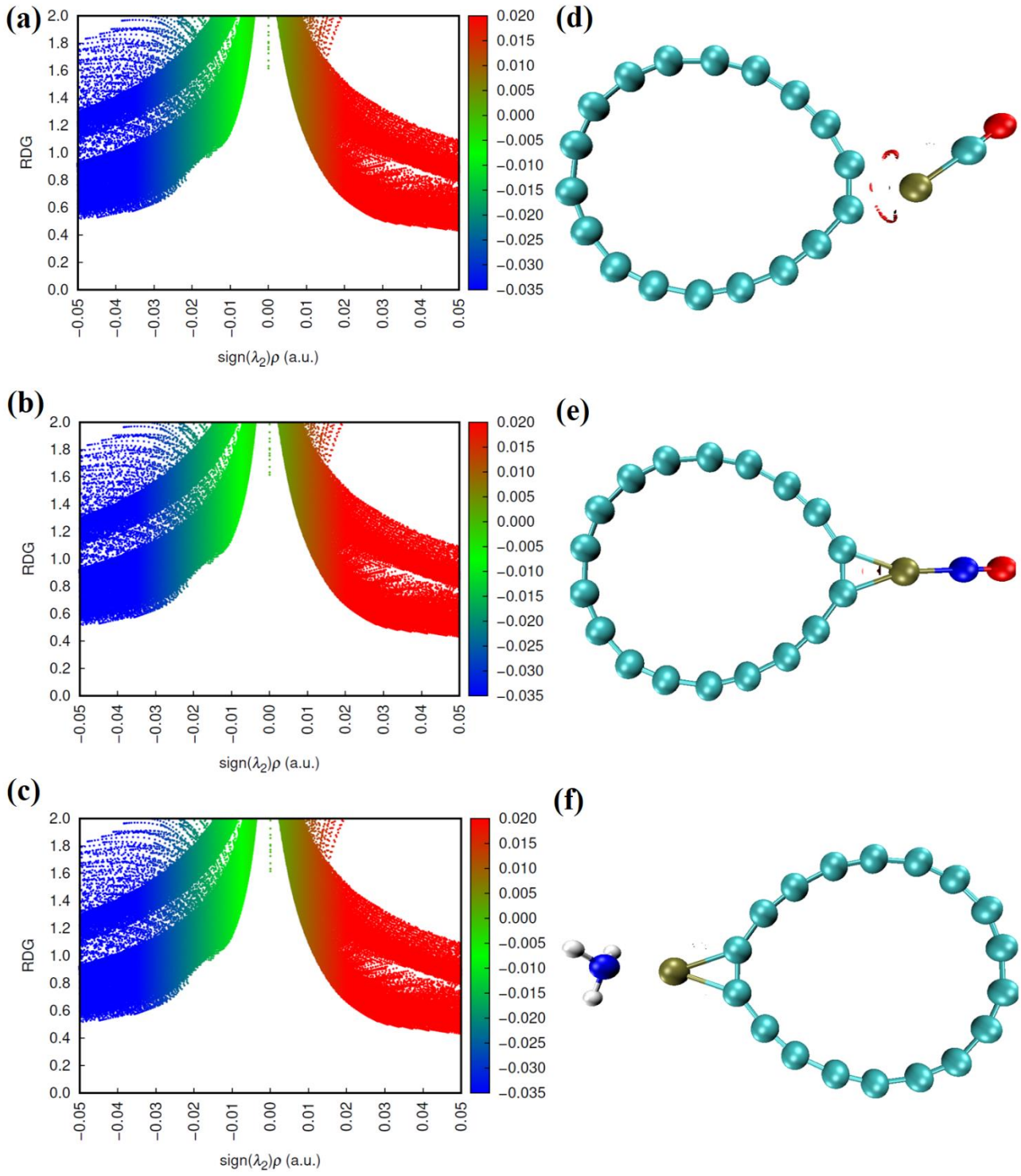

Figure 5.11: (a, b, c) reduced density gradient (RDG) plots and (d, e, f) non-covalent interaction (NCI) diagrams for $C_{18}Pt$ nanocluster after CO, NO, and NH_3 adsorption

5.3.6. Analysis of Raman Spectra

Raman spectroscopy serves as a non-invasive technique for characterizing nanostructures and getting into the subtle yet noticeable tag games of gas molecules and absorbers [23]. It's a gateway to in situ spectroscopic methods that unveil gas-phase composition and offer a qualitative analysis of the interplay between gas molecules and absorbers. Therefore, we simulated Raman spectra for $C_{18}TM$ nanoclusters both before and after gas adsorption, as depicted in *Figure 5.12*.

Beginning with the $C_{18}Ni$ nanocluster, an intense peak is indeed observed at a frequency of 60 cm^{-1}. Upon CO adsorption, this peak divides into two weak, somewhat fuzzy peaks. Following NO adsorption, once more, two blurred peaks emerge, with the first peak notably situated at 0 cm^{-1}. This specific occurrence aligns with experimental evidence, signifying an unshifted laser frequency, commonly referred to as the Rayleigh peak. An additional weak peak emerges at 1770 cm^{-1}, with its position shifting to the right after CO adsorption and to the left after NH_3 adsorption. An initial weak peak at 560 cm^{-1} is observable before adsorption, and it diminishes subsequently. However, in the context of NO adsorption, an extra peak becomes apparent at 1760 cm^{-1}, suggesting that weak intermolecular forces significantly influence the vibrational modes [24].

In the case of the $C_{18}Pd$ nanocluster, an intense peak at 64 cm^{-1} intensifies further during NH_3 adsorption. However, for the other two gases, it remains consistently intense even after adsorption. Twin peaks are discernible at 4064 cm^{-1}, and they intensify after CO adsorption but weaken following NH_3 adsorption. Conversely, during NO adsorption, the twin peaks further intensify. A Rayleigh peak [25] is additionally observed at 0 cm^{-1}. Two weak peaks are also identifiable in this context. The first is noted at 1890 cm^{-1}, which shifts to the right after CO adsorption, to the left after NH_3 adsorption, and intensifies following NO adsorption. The second weak peak, located at 2035 cm^{-1}, intensifies after CO and NH_3 adsorption but further weakens after NO adsorption. Finally, for the $C_{18}Pt$ nanocluster, the most intense peak is evident at 56 cm^{-1}. Following CO adsorption, this peak becomes blurred, while after NO adsorption, it intensifies. However, after NH_3 adsorption, it divides into three indistinct peaks. At 2070 cm^{-1}, a weak peak is present, which intensifies following CO and NH_3 adsorption and shifts to the right after NO adsorption. Another weak peak at 1820 cm^{-1} exhibits no significant change after the adsorption processes.

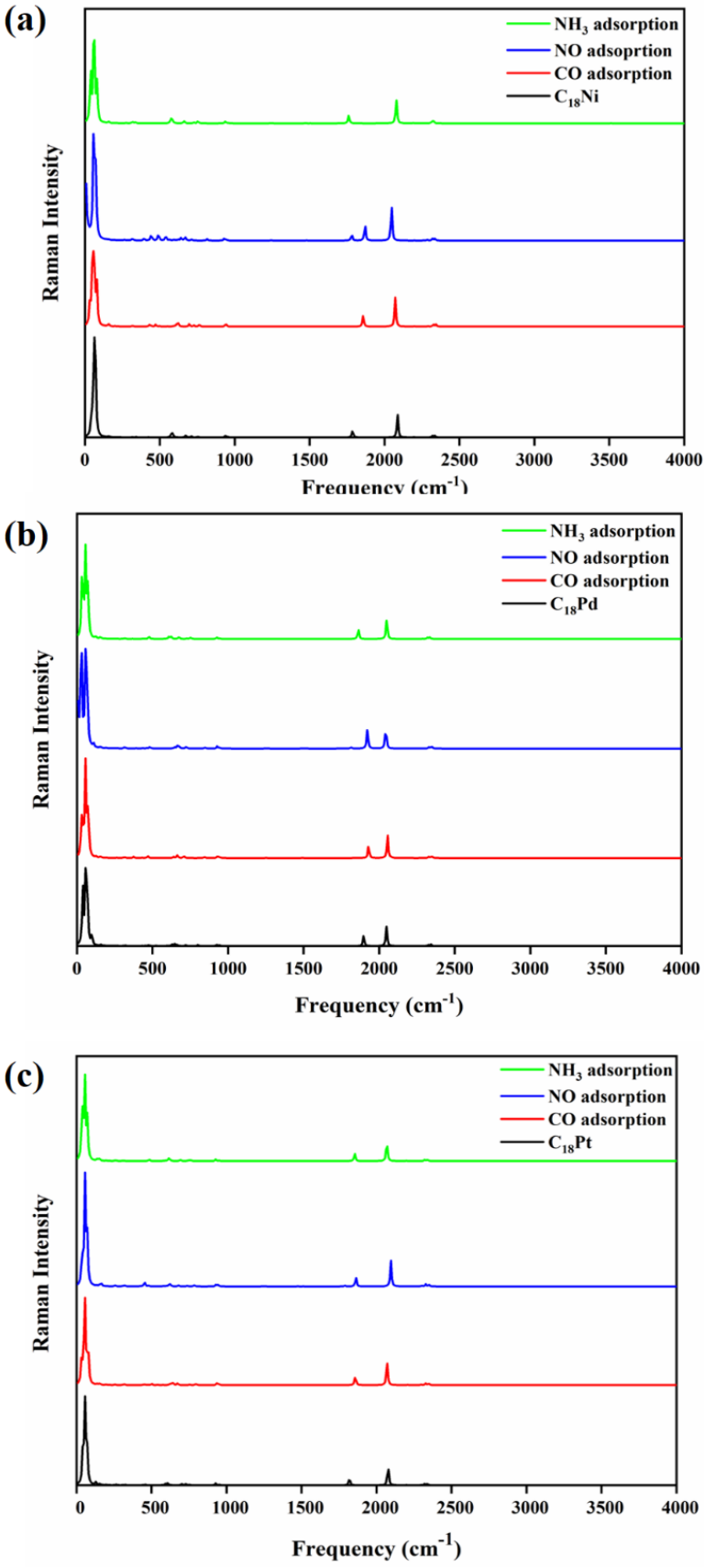

Figure 5.12: Raman spectra for (a) $C_{18}Ni$ (b) $C_{18}Pt$ (c) $C_{18}Pt$ nanocluster after CO, NO, and NH_3 adsorption

5.3.7. Sensing Response and Recovery Time

The sensing response of a material serves as an indicator of how its electrical conductivity undergoes alterations when it comes into contact with gas molecules or other substances that adhere to its surface. From an experimental perspective, the sensing response can be empirically associated with alterations in the current-voltage (I-V) characteristics of a system following the process of adsorption. These changes essentially signify variations in the material's electrical conductivity or resistivity. Theoretically, it is quantified through a parameter referred to as "S," which can be precisely determined by [26]:

$$S = exp(\frac{|\Delta E_G|}{K_B T}) \text{ ---- (4)}$$

ΔE_G denotes the change in energy associated with the adsorption process. K_B is the Boltzmann constant, T stands for temperature in Kelvin. In this work, nitric oxide (NO) interactions with $C_{18}Ni$ result in the highest S, signifying a potent sensing response, while the interactions of carbon monoxide (CO) and NO with $C_{18}Pt$ yield the lowest S values, indicating a comparatively subdued reactivity towards these gas molecules.

Recovery time (τ) represents the anticipated duration for an adsorbed molecule to desorb or detach from its host system. In sensor applications, a shorter recovery time is preferred for rapid and continuous monitoring. If the recovery time extends to several hours, the material is better suited for storage or removal purposes than sensing. This parameter is quantified using the formula [27]:

$$\tau = \upsilon^{-1}\, exp(\frac{-E_{ad}}{K_B T}) \text{ ---- (5)}$$

Where, *v* signifies the attempt frequency for desorption, set at 10^{-12} s^{-1}. E_{ad} is the adsorption energy. The computed recovery time (τ) is most prolonged for NO/$C_{18}Pd$ and briefest for NO/$C_{18}Ni$. However, for all cases involving CO, NO, and NH_3 over $C_{18}TM$, τ extends beyond several hours. This suggests that these nanoclusters are more suitable for storage or removal applications rather than sensors. *Table 5.4* presents the sensing response and recovery times of $C_{18}TM$ nanoclusters for CO, NO, and NH_3 adsorptions.

Table 5.4: sensing response and recovery times of C_{18}TM nanoclusters for CO, NO, and NH_3 adsorptions.

System	Sensing Response	Recovery Time (*s*)
CO/C_{18}Ni	47.86	1.83×10^{21}
NO/C_{18}Ni	5.06×10^{4}	2.06×10^{6}
NH_3/C_{18}Ni	4.69	4.92×10^{19}
CO/C_{18}Pd	3.43×10^{4}	8.46×10^{20}
NO/C_{18}Pd	487.51	6.42×10^{26}
NH_3/C_{18}Pd	3.87	4.39×10^{11}
CO/C_{18}Pt	0.99	1.09×10^{14}
NO/C_{18}Pt	0.99	2.61×10^{19}
NH_3/C_{18}Pt	6.92	2.34×10^{21}

5.3.8. Comparison with the Pristine and Doped C_{18} Nanoclusters

Based on our previous research as well as the findings in this study, it is evident that among all the nanoclusters examined, transition metal-decorated C_{18} nanoclusters (C_{18}TM) exhibit significant potential for the removal of CO, NO, and NH_3 gas molecules. This conclusion is primarily drawn from their notably negative adsorption energies.

In the case of the Nitrogen-substituted C_{18} nanocluster (C_{17}B), its suitability for CO and NH_3 sensing is limited due to less negative adsorption energies and adsorption distances exceeding 3 Å. C_{17}B nanocluster, on the other hand, proves to be an effective choice for removal applications, thanks to its highly negative adsorption energies.

As for the pristine C_{18} nanocluster, it emerges as a promising candidate for "ultra-fast" gas sensors, characterized by optimal adsorption distances and recovery times in the nanosecond range. This work underscores the potential usefulness of these nanoclusters in addressing specific gas sensing and removal applications.

Table 5.5: Adsorption energies and distances of C_{18}TM as compared to the Pristine and Doped C_{18} Nanoclusters

System	CO adsorption		NO adsorption		NH_3 adsorption		Ref.
	E_{ad} (eV)	d (Å)	E_{ad} (eV)	d (Å)	E_{ad} (eV)	d (Å)	
C_{18}Ni	-1.98	1.78	-1.96	1.72	-1.89	1.98	This work
C_{18}Pd	-1.55	1.72	-1.09	1.95	-1.41	2.20	
C_{18}Pt	-2.31	1.89	-1.87	1.87	-1.99	2.14	
Pristine C_{18}	-0.31	1.43	-0.29	1.43	-0.23	2.85	[28]
C_{17}B	-1.41	1.51	-2.00	1.42	-1.81	1.59	[29]
C_{17}N	-0.15	4.28	-1.32	1.49	-0.25	3.41	

5.4. CONCLUSION

In this chapter, we conducted a comprehensive investigation of the structural, electronic, topological, spectroscopic, and sensing properties of C_{18}TM nanoclusters in their interactions with the toxic gases CO, NO, and NH_3. The computed adsorption energies consistently demonstrated strong affinity, with highly negative values observed across all cases. Notably, we observed a substantial sensing response, particularly for NO over C_{18}Ni and CO over C_{18}Pd nanoclusters, underlining their potential utility in conductivity-based sensors. The Quantum Theory of Atoms in Molecules (QTAIM) unveiled the strength of each interaction, providing valuable insights into the nature of bonding within these systems.

Similarly, our analysis of Raman spectra shed light on the vibrational characteristics associated with these interactions. Additionally, the Non-Covalent Interaction (NCI) analysis aptly delineated the mechanisms of van der Waals interactions. An interesting finding relates to the extended recovery times observed in our calculations, which can be attributed to the highly negative adsorption energies. This prolonged desorption time suggests that C_{18}TM nanoclusters are better suited for the removal of CO, NO, and NH_3 gases rather than as quick-response sensors.

BIBLIOGRAPHY:

[1] L. M. Scriven, K. Kaiser, F. Schulz and A. J. Sterling, 2020, 1–19.

[2] K. Kaiser, L. M. Scriven, F. Schulz, P. Gawel, L. Gross and H. L. Anderson, *Science (80-.).*, 2019, **365**, 1299–1301.

[3] M. D. Esrafili and H. Janebi, *Mol. Phys.*, 2020, **118**, 1–9.

[4] Y. Peng and J. Li, *Front. Environ. Sci. Eng.*, 2013, **7**, 403–411.

[5] J. Panchal, A. Gauswami, D. Chodvadiya, H. Jadeja and P. K. Jha, 2024, **311**, 1–5.

[6] S. Patel, P. Patel, D. Chodvadiya, N. N. Som and P. K. Jha, *J. Mol. Liq.*, 2022, **352**, 3–4.

[7] S. Lakshmy, S. Joseph, G. Sanyal, N. Kalarikkal and B. Chakraborty, *J. Appl. Phys.*, 2022, **132**, 184303.

[8] M. J. Frisch, Trucks, G.W., Schlegel, H.B., Scuseria, G.E., Robb, M.A., Cheeseman, J.R., *Gaussian 09, Revis. A.02, Gaussian, Inc.*, 2016, 1–2.

[9] Z. Liu, T. Lu and Q. Chen, *Carbon N. Y.*, 2020, **165**, 461–467.

[10] S. Chiodo, N. Russo and E. Sicilia, *J. Chem. Phys.*, 2006, **125**, 1–8.

[11] W. Humphrey, A. Dalke and K. Schulten, *J. Mol. Graph.*, 1996, **14**, 33–38.

[12] T. Lu and F. Chen, *J. Comput. Chem.*, 2012, **33**, 580–592.

[13] N. R. Sheela, S. Muthu and S. Sampathkrishnan, *Spectrochim. Acta - Part A Mol. Biomol. Spectrosc.*, 2014, **120**, 237–251.

[14] J. Mawwa, S. U. D. Shamim, S. Khanom, M. K. Hossain and F. Ahmed, *RSC Adv.*, 2021, **11**, 32810–32823.

[15] S. Vadalkar, D. Chodvadiya, K. N. Vyas and P. K. Jha, *Mater. Today Proc.*, 2022, **67**, 229–237.

[16] V. Nagarajan and R. Chandiramouli, *Comput. Theor. Chem.*, 2019, **1150**, 63–70.

[17] R. F. W. Bader, *Acc. Chem. Res.*, 1985, **18**, 9–15.

[18] S. J. Grabowski, *J. Mol. Model.*, 2013, **19**, 4713–4721.

[19] A. R. Azady, S. Ahmed and S. Islam, 2021, **2249**, 68–79.

[20] X. Niu, Z. Huang, L. Ma, T. Shen and L. Guo, *J. Chem. Sci.*, 2013, **125**, 949–958.

[21] F. Akman, N. Issaoui and A. S. Kazachenko, *J. Mol. Model.*, 2020, **26**, 12974–12980.

[22] T. Jenkins, K. Berland and T. Thonhauser, 2021, 3–7.

[23] V. Sharma, N. N. Som, S. B. Pillai and P. K. Jha, *Spectrochim. Acta - Part A Mol. Biomol. Spectrosc.*, 2020, **224**, 2020–2023.

[24] R. Ludwig, K. Fumino, 2014, **192**, 94-102.

[25] M. H. Brooker, O. F. Nielsen and E. Praestgaard, 1988, **12**, 71–78.

[26] N. A. Tukadiya, S. K. Jana, B. Chakraborty and P. K. Jha, *Surfaces and Interfaces*, 2023, **41**, 1–16.

[27] S. Peng, K. Cho, P. Qi and H. Dai, *Chem. Phys. Lett.*, 2004, **387**, 271–276.

[28] S. Vadalkar, D. Chodvadiya, N. N. Som, K. N. Vyas, P. K. Jha and B. Chakraborty, *ChemistrySelect*, 2022, **7**, e202103874.

[29] S. Vadalkar, D. Chodvadiya, N. N. Som, K. N. Vyas and P. K. Jha, *ChemistrySelect*, 2023, **8**, e202204862.